Supplementary Materials and Methods to: Mitochondrial Inhibitor Atovaquone Increases Tumor Oxygenation and Inhibits Hypoxic Gene Expression in Patients with Non-Small Cell Lung Cancer

ADDITIONAL DESCRIPTION OF METHODOLOGY

Defining response to atovaquone using hypoxia PET-CT

≥10% reduction in hypoxic volume from baseline as measured by FMISO or FAZA PET-CT was classed as a meaningful reduction following atovaquone treatment. This cut-off was based on FMISO reproducibility test-retest data and used the minimum detectable change (MDC) method (1). Okamoto *et al*. demonstrated a mean difference of 2.7% and standard deviation 14% in tumor-to-muscle (TMR) volumes from FMISO scans repeated within 48 hours (n=9, excluding two patients with TMR volumes <1.5 mL) (2). MDC is the minimum change at 95% confidence and is defined as the standard error (4.7) multiplied by 1.96, giving 9.2%. The ≥10% reduction in HV threshold was previously ratified by the University's Independent Early Phase Trial Oversight Committee in combination with external radiology advice and we have recently published another clinical study using this threshold (3).

Dynamic hypoxia PET

Dynamic hypoxia PET analysis was conducted to assess tumor hypoxia and perfusion using the dynamic, 2- and 4-hour 10 minute FMISO or FAZA PET acquisitions as previously described by McGowan *et al* (4). In brief, tumor and blood time activity curves were extracted from the rigidly registered PET images and fitted to an irreversible three-tissue compartmental model. From this, the volume of blood in tumor (v_B), rate of FMISO flow from blood to interstitial space (K_1) and rate of FMISO binding (k_5) were extracted for each

patient pre- and post-atovaquone treatment. v_B and K_1 are associated with tumor perfusion and k_5 with tumor hypoxia.

Perfusion CT

Perfusion (pCT) was performed immediately following the 4-hour hypoxia PET acquisition with patients in the same position. A pre-contrast CT was initially performed to determine the location for the pCT scan. The pCT was limited to a 4 cm region of the tumor in the superior to inferior direction due to high temporal resolution (one image per second) and CT detector width. This meant that for large tumors the tumor was not fully imaged during the scan. When the change in pCT parameters was investigated between imaging visits per individual patient, only data from matched tumor regions was used. Images were acquired in cine mode (120 kV, 60 mA) with 70 mL iodinated contrast (Omnipaque 300) injected at 5 mL/s followed by a 25 mL water flush at 5 mL/s. The scan duration was 45 seconds, during which time patients were instructed to hold their breath in inspiration. As any movement during the scan is of concern for pCT analysis since the x/y voxel size is very small (0.7 mm), motion correction was performed using software developed by our Engineering Department (5). The motion-corrected pCT data was then processed voxel-by-voxel using commercial software GE Perfusion 4D (GE Healthcare, USA) with an input function obtained from the mean of a selected region in the descending aorta to provide tumor blood flow (BF), blood volume (BV) and mean transit time (MTT) parameters. A meaningful change in these parameters was classed as ≥25% change from baseline, consistent with previously published data (6).

MRI analysis

MRI data was acquired on a 3T MR750 GE scanner (GE Healthcare, USA). DCE MRI data was obtained using a proprietary LAVA sequence with Prohance given in a bolus during a

free-breathing, non-gated protocol. The data was processed using Quantiphyse (www.quantiphyse.org) to correct for respiratory motion (7) and obtain perfusion values. The mean K^{trans} value within the tumor ROI was calculated by the DCE Modelling widget using the Tofts' model (8) and population-based arterial input function (9). Quantitative relaxation parameters were imaged in a single slice through the center of the tumor. T2* values were obtained using the StarMap sequence and processing tool (GE Healthcare, USA), and T1 values using a shMOLLI sequence. ROI's were drawn on a T2-weighted, high-resolution image and then registered to the quantitative data sets using in-house MATLAB software (MathWorks, USA).

Tumor pimonidazole, CD31 and CD146 immunohistochemistry and imaging analysis

Immunohistochemistry for pimonidazole, CD31 and CD146 was conducted, whenever possible, from multiple tumor blocks taken from three equally spaced entire tumor cross sections. 4 μM sections were generated from each block and stained using a Leica BOND-MAX autostainer (Leica Biosystems, Germany) to ensure high-throughput and technical consistency. The following conditions were used: antigen retrieval at 100ºC for 20 minutes with Epitope Retrieval Solution 1 for pimonidazole and Epitope Retrieval Solution 2 for CD31 and CD146 (both from Leica Biosystems, Germany), primary antibody incubation for 30 minutes and then detection using horseradish peroxidase enzyme-based BOND Polymer Refine Detection System (Leica Biosystems, Germany), as per manufacturer's instructions. The primary antibodies used were Hypoxyprobe-1 MAb1 anti-pimonidazole mouse monoclonal antibody (4.3.11.3; Pharmacia International, USA) at 1/1000 dilution, JC70A anti-CD31 mouse monoclonal antibody (M0823; Agilent, UK) at 1/800 dilution and EPR3208 anti-CD146 rabbit monoclonal antibody (ab75769; Abcam, UK) at 1/500 dilution. For positive controls, a mouse xenograft pilot 1 L1 model treated with pimonidazole

(Department of Oncology, University of Oxford, UK) and human tonsil were used. Negative control samples were sections from the same control tissues incubated with either a mouse (ab37355; Abcam, UK) or rabbit (GTX47478; GeneTex, UK) isotype control antibody at the same concentration as the matched primary antibody. The quality of staining was reviewed and approved by an experienced lung cancer histopathologist (M.M.). Due to the large number of slides, an automated scoring method was developed to ensure high-throughput and consistent scoring. Stained slides were scanned at x20 objective magnification using a NanoZoomer S210 digital slide scanner (Hamamatsu, Japan) to generate digital whole slide images. All subsequent analyses were performed in MATLAB (MathWorks, USA), using custom-made analysis scripts, and were conducted blind to treatment allocation. Following manual demarcation of the edge of the tissue section, tumor boundary and any areas of processing artefact, detection of positively stained tissue was undertaken at x2.5 objective magnification using a bespoke imaging pipeline. This pipeline used the Simple Linear Iterative Clustering (SLIC) algorithm (10) to generate superpixels with a size of approximately 30 pixels per superpixel. A support vector machine (SVM) classifier was then used to distinguish positively stained from negatively stained superpixels. The SVM classifier was trained by manual annotation of regions of positive and negative staining within images from a number of different patients that were deemed representative of staining patterns observed across the entire cohort. The proportion of stained tissue within the annotated tumor region, without differentiation of scoring between the tumor epithelial and stromal compartments, was reported as a percentage score per tumor block, per tumor cross section and per whole tumor and output images were visually checked to confirm accuracy of classification. This approach permits direct comparison with hypoxia PET-CT data and is routine practice in histopathology studies (11).

Tumor RNA extraction for RNAseq analysis

RNA isolation was performed using RecoverAll Total Nucleic Acid Isolation Kit for FFPE (Invitrogen, USA), as per manufacturer's instructions. Briefly, 10 μm thick sections from, whenever possible, three equally spaced entire tumor cross sections were deparaffinized by xylene treatment at 50ºC, washed with ethanol and protease digested for 15 minutes at 50ºC and then overnight at 80ºC. RNA was isolated from 200 μL of lysate by column purification. RNA yield and integrity were assessed using the Agilent 2100 Bioanalyzer system and associated RNA 6000 Nano Chip (Agilent Technologies, USA). The average RNA Integrity Number was approximately 3 across all samples and RNA lengths were typically >200 base pairs.

Plasma collection

For each patient, 2 x 10 mL EDTA vacutainers were filled with blood, inverted a number of times and placed on ice with subsequent processing occurring within 30 minutes. The samples were centrifuged at 2000 x g for 10 minutes at 4°C after which the plasma layer was transferred into fresh collection tubes and centrifuged again at the same conditions. The plasma was then aliquoted into cryovials and stored at -80°C.

Measurement of plasma VEGF, CAIX and osteopontin

Frozen plasma samples were defrosted, mixed and spun before being assayed using Human Carbonic Anhydrase IX, VEGF or Osteopontin Quantikine ELISA Kits (R&D Systems, USA, DCA900, DVE00 and DOST00, respectively) according to the manufacturer's instructions. Samples were assayed in duplicate alongside seven standards (prepared on the day) and three quality controls (QCs) generated previously from recombinant protein (R&D Systems, USA). One set of standards and two sets of QCs were assayed for each 96 well

plate. Plates were measured for absorbance at 450 and 570 nm using the FLUOstar Omega Plate Reader (BMG LABTECH, Germany). Blank corrected readings at 570 nm were subtracted from blank corrected readings at 450 nm using MARS Data Analysis Software (BMG LABTECH, Germany). MasterPlex Readerfit Software (MiraiBio Group of Hitachi Solutions America, Ltd) was used to generate a 4-parameter fit curve (weighted with $1/y^2$) from the blank corrected 450-570 nm subtracted MARS data to determine concentration values from optical density. Mean concentration, standard deviation and percentage coefficient of variation (%CV) were generated for each duplicate. The mean value of at least 4 of 6 QC concentrations on each plate were required to be within 20% (for high and medium QC) or 25% (for low QC) of the expected concentration. In addition, for the standards the mean readings needed to be within 15% of expected value, except for the lowest standard, which needed to be within 25%. A greater than 25% increase or decrease in plasma VEGF, CAIX or osteopontin was deemed a meaningful change in analyte between trial visits, a widely accepted margin for error when measuring changes in plasma protein levels using this technique.

Measurement of plasma miR-210

RNA was purified from 500 µl cleared plasma using the Quick-cfRNA serum & plasma kit (Zymo Research), as per manufacturer's instructions, with one additional step prior proteinase K digestion, which involved a 15-minute incubation at 55°C of the cleared plasma samples to improve subsequent proteinase K digestion. A synthetic spike-in miRNA, miR-Cel-39, (Thermo Fisher Scientific) was added to the plasma samples prior to processing to allow for correction of differences in RNA extraction efficiencies between samples. Purified RNA was subjected to cDNA synthesis using the TaqMan microRNA reverse transcription kit and miRNA specific primers for hsa-miR-210, hsa-miR-16 and cel-miR-39 (TaqMan

MicroRNA Assays, Thermo Fisher Scientific) in singleplex reactions using 1/12 of the eluted RNA for each reaction. TaqMan PCR was performed in duplicate singleplex reactions using primers and probes from the same TaqMan MicroRNA assay kits, TaqMan Universal Master Mix II and 1/10 of the cDNA for each PCR reaction. The relative miR-210 expression in each plasma sample was determined using the delta-delta Ct method using the spike-in (Cel-miR-39) and the endogenous (miR-16) miRNAs as combined reference miRNAs.

Measurement of plasma atovaquone levels

Atovaquone in plasma was measured using a validated high-performance liquid chromatography (HPLC) method with absorbance detection. Atovaquone standard was supplied by Toronto Research Chemicals Inc, Canada and 2-tertbutyl anthraquinone (internal standard - IS) was supplied by Sigma-Aldrich, UK. All solvents were supplied from Fisher Scientific, USA. Control human EDTA plasma was obtained from Seralab/BioIVT.

Stocks solutions of atovaquone were prepared in DMSO (5 mM) and then further dilutions were carried out in control human EDTA plasma to prepare calibration curves with the range of 2 to 200 µM. QCs were also prepared at concentrations of 6, 80 and 160 µM. IS stock solutions were prepared in acetonitrile (5 mM) and then further diluted in acetonitrile to prepare a working solution of 100 µM.

20 µL calibration standards, QCs and patient plasma was aliquoted into polypropylene tubes for analysis. 20 µL IS was added to each tube and mixed followed by 180 µL LC-MS grade methanol with mixing for 10 seconds. Protein precipitates were removed by centrifuging (18000 x g, 4 °C, 10 minutes). The supernatant was transferred to HPLC vials for measuring.

HPLC analysis was carried out on a Waters e2695 separations module with an incubation temperature of 15 °C. Separation was achieved on a Phenomenex Gemini, C6 Phenyl 3 µm,

150 x 3 mm column with a Phenomenex Gemini, C6 Phenyl 3 µm, 4 x 2 mm guard cartridge maintained at 35 °C. Samples (10 µL) were eluted in A: 0.1 % formic acid, B: LC-MS grade methanol with a flow rate of 0.6 ml/minute, and a linear gradient of 85-100 % B in 6 minutes, stepped down to 50 % B for 1 minute, returning to starting conditions in 0.1 minute, total run time 12 minutes. Analytes were detected by absorbance spectrometry with a Waters 2996 photodiode array detector, measuring at 250 nm. Atovaquone had a retention time of 4.5 minutes and IS had a retention time of 3.8 minutes.

SUPPLEMENTARY FIGURE

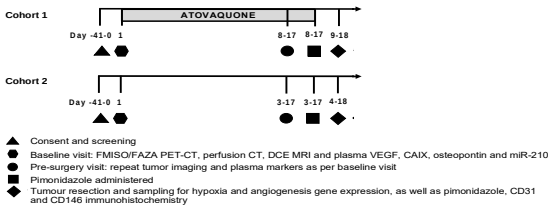

Figure S1. Trial schema**.**

SUPPLEMENTARY TABLES

Table S1. List of genes in hypoxia signatures.

Buffa (12)	**Harris** (13)	**Hallmark** (14)	**Winter** (15)
ACOT7	ADM	ADM	ABCB1
ADM	AK3	ADORA2B	ACAT1
AK3L1	ALDOA	AK4	ADM
ALDOA	ANGPT2	AKAP12	ADORA2B
ANKRD37	APEX1	ALDOA	AK2
ANLN	BHLHE40	ALDOB	AK3
BNIP3	BIK	ALDOC	ALDH1A1
C20orf20	BNIP3	AMPD3	ALDH1A3
CA9	BNIP3L	ANGPTL4	ALDOA
CDKN3	CA12	ANKZF1	ALDOC
CHCHD2	CA9	ANXA2	ANGPT2
CORO1C	CCL2	ATF3	ANGPTL4
CTSL2	CCNG2	ATP7A	ANXA1
DDIT4	CD99	B3GALT6	ANXA2
ENO1	CDKN1A	B4GALNT2	ANXA5
ESRP1	CDKN1B	BCAN	ARHGAP5
GAPDH	COL5A1	BCL2	ARSE
GPI	CP	BGN	ART1
HIG2	DDIT3	BHLHE40	BACE2
HK2	EDN1	BNIP3L	BATF3
KIF20A	EDN2	BRS3	BCL2L1
KIF4A	ENO1	BTG1	BCL2L2
LDHA	ENPEP	CA12	BHLHE40
LRRC42	EPAS1	CASP6	BHLHE41
MAD2L2	EPO	CAV1	BIK
MAP7D1	F3	CCNG2	BIRC2
MCTS1	FGF3	CCRN4L	BNIP3
MIF	FLT1	CDKN1A	BNIP3L
MRPL13	FOS	CDKN1B	BPI
MRPL15	FTL	CDKN1C	BTG1
MRPS17	GAPDH	CHST2	C11orf2
NDRG1	HDAC9	CHST3	C7orf68
NP	HGF	CITED2	CA12
P4HA1	HIF1A	COL5A1	CA9
PFKP	HK1	CP	CALD1
PGAM1	HK2	CSRP2	CCNG2

PGK1	HMOX1	CTGF	CCT6A
PSMA7	IGF2	CXCR4	CD99
PSRC1	IGFBP1	CXCR7	CDK1
SEC61G	IGFBP2	CYR61	CDKN1A
SHCBP1	IGFBP3	DCN	CDKN1B
SLC16A1	IL6	DDIT3	CITED2
SLC25A32	IL8	DDIT4	CLK1
SLC2A1	JUN	DPYSL4	CNOT7
TPI1	L1CAM	DTNA	COL4A5
TUBA1B	LDHA	DUSP1	COL5A1
TUBA1C	LRP8	EDN2	COL5A2
TUBB6	MIF	EFNA1	COL5A3
UTP11L	MMP13	EFNA3	CP
VEGFA	NFKB1	EGFR	CTSD
YKT6	P4HA1	ENO1	CXCR4
	PDGFB	ENO2	D4S234E
	PFKL	ENO3	DDIT3
	PFKP	ERO1L	DEC1
	PGF	ERRFI1	DDIT4
	PGK1	ETS1	DKC1
	PKM2	EXT1	DR1
	PLAUR	F3	EDN1
	PRPS1	FAM162A	EDN2
	PTGS2	FBP1	EFNA1
	RP1	FOS	EGF
	SAT1	FOSL2	EGR1
	SLC2A1	FOXO3	EIF4A3
	SLC2A3	GAA	ELF3
	SPP1	GALK1	ELL2
	STC1	GAPDH	ENG
	TAGLN	GAPDHS	ENO1
	TEK	GBE1	ENO3
	TF	GCK	ENPEP
	TFF3	GCNT2	EPO
	TFRC	GLRX	ERRFI1
	TGFA	GPC1	ETS1
	TGFB1	GPC3	F3
	TGFB3	GPC4	FABP5
	TGM2	GPI	FGF3
	TH	GRHPR	FKBP4
	TXN	GYS1	FLT1

	VEGFA	HAS1	FN1
	VIM	HDLBP	FOS
	XRCC5	HEXA	FTL
	XRCC6	HK1	GAPDH
		HK2	GBE1
		HMOX1	GLRX
		HOXB9	GPI
		HS3ST1	GPRC5A
		HSPA5	HAP1
		IDS	HBP1
		IER3	HDAC1
		IGFBP1	HDAC9
		IGFBP3	HERC3
		IL6	HERPUD1
		ILVBL	HGF
		INHA	HIF1A
		IRS2	HK1
		ISG20	HK2
		JMJD6	HLA-DQB1
		JUN	HMOX1
		KDELR3	HMOX2
		KDM3A	HSPA5
		KIF5A	HSPD1
		KLF6	HSPH1
		KLF7	HYOU1
		KLHL24	ICAM1
		LALBA	ID2
		LARGE	IFI27
		LDHA	IGF2
		LDHC	IGFBP1
		LOX	IGFBP2
		LXN	IGFBP3
		MAFF	IGFBP5
		MAP3K1	IL6
		MIF	IL8
		MT1E	INSIG1
		MT2A	IRF6
		MXI1	ITGA5
		MYH9	JUN
		NAGK	KDR
		NCAN	KRT14

		NDRG1	KRT18
		NDST1	KRT19
		NDST2	LDHA
		NEDD4L	LDHB
		NFIL3	LEP
		NR3C1	LGALS1
		P4HA1	LONP1
		P4HA2	LOX
		PAM	LRP1
		PCK1	MAP4
		PDGFB	MET
		PDK1	MIF
		PDK3	MMP13
		PFKFB3	MMP2
		PFKL	MMP7
		PFKP	MPI
		PGAM2	MT1L
		PGF	MTL3P
		PGK1	MUC1
		PGM1	MXI1
		PGM2	NDRG1
		PHKG1	NFIL3
		PIM1	NFKB1
		PKLR	NFKB2
		PKP1	NOS1
		PLAC8	NOS2
		PLAUR	NOS2P1
		PLIN2	NOS2P2
		PNRC1	NOS3
		PPARGC1A	NR3C1
		PPFIA4	NR4A1
		PPP1R15A	NT5E
		PPP1R3C	ODC1
		PRDX5	P4HA1
		PRKCA	P4HA2
		PRKCDBP	PAICS
		PTRF	PDGFB
		PYGM	PDK3
		RBPJ	PFKFB1
		RORA	PFKFB3
		RRAGD	PFKFB4

		S100A4	PFKL
		SAP30	PGAM1
		SCARB1	PGF
		SDC2	PGK1
		SDC3	PGK2
		SDC4	PGM1
		SELENBP1	PIM1
		SERPINE1	PIM2
		SIAH2	PKM2
		SLC25A1	PLAU
		SLC2A1	PLAUR
		SLC2A3	PLIN2
		SLC2A5	PLOD2
		SLC37A4	PNN
		SLC6A6	PNP
		SRPX	POLM
		STBD1	PPARA
		STC1	PPAT
		STC2	PROK1
		SULT2B1	PSMA3
		TES	PSMD9
		TGFB3	PTGS1
		TGFBI	PTGS2
		TGM2	QSOX1
		TIPARP	RBPJ
		TKTL1	RELA
		TMEM45A	RIOK3
		TNFAIP3	RNASEL
		TPBG	RPL36A
		TPD52	RRP9
		TPI1	SAT1
		TPST2	SERPINB2
		UGP2	SERPINE1
		VEGFA	SGSM2
		VHL	SIAH2
		VLDLR	SIN3A
		WISP2	SIRPA
		WSB1	SLC16A1
		XPNPEP1	SLC16A2
		ZFP36	SLC20A1
		ZNF292	SLC2A1

			SLC2A3
			SLC3A2
			SLC6A10P
			SLC6A16
			SLC6A6
			SLC6A8
			SORL1
			SPP1
			SRSF6
			SSSCA1
			STC2
			STRA13
			SYT7
			TBPL1
			TCEAL1
			TEK
			TF
			TFF3
			TFRC
			TGFA
			TGFB1
			TGFB3
			TGFBI
			TGM2
			TH
			THBS1
			THBS2
			TIMM17A
			TNFAIP3
			TP53
			TPBG
			TPD52
			TPI1
			TXN
			TXNIP
			UMPS
			VEGFA
			VEGFB
			VEGFC
			VIM
			VPS11

			XRCC6

Table S2. List of genes in glycolysis, oxidative phosphorylation and reactive oxygen species signatures.

KEGG GLYCOLYSIS[a]	KEGG OXPHOS[b]	ROS GO1[c]	ROS GO 2[d]	Hallmark ROS[e]
ACSS1	ATP12A	ABL1	ABL1	ABCC1
ACSS2	ATP4A	ADA	ADPRHL2	ATOX1
ADH1A	ATP4B	ADAM9	AGAP3	CAT
ADH1B	ATP5F1A	ADPRHL2	AIFM1	CDKN2D
ADH1C	ATP5F1B	AGAP3	AKR1C3	EGLN2
ADH4	ATP5F1C	AIFM1	AKT1	ERCC2
ADH5	ATP5F1D	AKR1C3	ANKZF1	FES
ADH6	ATP5F1E	AKT1	ANXA1	FTL
ADH7	ATP5MC1	ANKZF1	APEX1	G6PD
AKR1A1	ATP5MC1P5	ANXA1	APOA4	GCLC
ALDH1A3	ATP5MC2	APEX1	AQP1	GCLM
ALDH1B1	ATP5MC3	APOA4	ARG1	GLRX
ALDH2	ATP5ME	APOD	ATP7A	GLRX2
ALDH3A1	ATP5MF	APOE	AXL	GPX3
ALDH3A2	ATP5MG	APTX	BECN1	GPX4
ALDH3B1	ATP5PB	AQP1	BMP7	GSR
ALDH3B2	ATP5PD	AREG	BNIP3	HHEX
ALDH7A1	ATP5PF	ARG1	BTK	HMOX2
ALDH9A1	ATP5PO	ATP7A	CAMKK2	IPCEF1
ALDOA	ATP6AP1	AXL	CBX8	JUNB
ALDOB	ATP6V0A1	BAD	CCNA2	LAMTOR5
ALDOC	ATP6V0A2	BAK1	CCS	LSP1
BPGM	ATP6V0A4	BCL2	CD36	MBP
DLAT	ATP6V0B	BECN1	CDK1	MGST1
DLD	ATP6V0C	BMP7	CDK2	MPO
ENO1	ATP6V0D1	BNIP3	CFLAR	MSRA
ENO2	ATP6V0D2	BTK	CHUK	NDUFA6
ENO3	ATP6V0E1	CAMKK2	CRK	NDUFB4
FBP1	ATP6V0E2	CAPN2	CRYGD	NDUFS2
FBP2	ATP6V1A	CASP3	CYP1B1	NQO1
G6PC	ATP6V1B1	CAT	DHFR	OXSR1
G6PC2	ATP6V1B2	CBX8	DHFRP1	PDLIM1
GALM	ATP6V1C1	CCL19	DNM2	PFKP
GAPDH	ATP6V1C2	CCNA2	DPEP1	PRDX1
GCK	ATP6V1D	CCR7	ECT2	PRDX2
GPI	ATP6V1E1	CCS	EGFR	PRDX4
HK1	ATP6V1E2	CD36	ENDOG	PRDX6

HK2	ATP6V1F	CDK1	ERCC6L2	PRNP
HK3	ATP6V1G1	CDK2	ETS1	PTPA
LDHA	ATP6V1G2	CFLAR	EZH2	SBNO2
LDHAL6A	ATP6V1G3	CHUK	FABP1	SCAF4
LDHAL6B	ATP6V1H	COA8	FANCC	SELENOS
LDHB	COX10	COL1A1	FBLN5	SOD1
LDHC	COX11	CRK	FER	SOD2
PCK1	COX15	CRYAB	FOS	SRXN1
PCK2	COX17	CRYGD	FOXO1	STK25
PDHA1	COX4I1	CYP1B1	FXN	TXN
PDHA2	COX4I2	CYP2E1	GCH1	TXNRD1
PDHB	COX5A	DHFR	GLRX2	TXNRD2
PFKL	COX5B	DHFRP1	GPR37	
PFKM	COX6A1	DNM2	GPR37L1	
PFKP	COX6A2	DPEP1	GUCY1B1	
PGAM1	COX6B1	DUSP1	HDAC2	
PGAM2	COX6B2	ECT2	HDAC6	
PGAM4	COX6C	EDN1	HGF	
PGK1	COX6CP3	EEF2	HNRNPD	
PGK2	COX7A1	EGFR	HSF1	
PGM1	COX7A2	EGLN1	IL10	
PGM2	COX7A2L	ENDOG	IL18RAP	
PKLR	COX7B	ERCC6	IL6	
PKM	COX7B2	ERCC6L2	IMPACT	
TPI1	COX7C	ETS1	JUN	
	COX8A	EZH2	KCNC2	
	COX8C	FABP1	KDM6B	
	CYC1	FANCC	KLF2	
	LHPP	FBLN5	KLF4	
	MT-ATP6	FER	LCN2	
	MT-ATP8	FKBP1B	LRRK2	
	MT-CO1	FOS	MAP1LC3A	
	MT-CO2	FOSL1	MAP3K5	
	MT-CO3	FOXO1	MAPK1	
	MT-CYB	FXN	MAPK13	
	MT-ND1	FYN	MAPK3	
	MT-ND2	GCH1	MAPK7	
	MT-ND3	GLRX2	MAPK8	
	MT-ND4	GNAO1	MAPK9	
	MT-ND4L	GPR37	MAPT	
	MT-ND5	GPR37L1	MDM2	
	MT-ND6	GPX1	MET	
	NDUFA1	GSTP1	MIR103A1	
	NDUFA10	GUCY1B1	MIR103A2	
	NDUFA11	HBA1	MIR107	
	NDUFA2	HBA2	MIR133A1	

	NDUFA3	HBB	MIR133A2	
	NDUFA4	HDAC2	MIR17	
	NDUFA4L2	HDAC6	MIR21	
	NDUFA5	HGF	MIR34A	
	NDUFA6	HMOX1	MIR92A1	
	NDUFA7	HNRNPD	MIR92A2	
	NDUFA8	HP	MIRLET7B	
	NDUFA9	HSF1	MMP2	
	NDUFAB1	HYAL1	MMP3	
	NDUFB1	HYAL2	MMP9	
	NDUFB10	IL10	MPO	
	NDUFB2	IL18RAP	MPV17	
	NDUFB3	IL6	MT3	
	NDUFB4	IMPACT	MTR	
	NDUFB5	JUN	MYB	
	NDUFB6	KCNA5	NCF1	
	NDUFB7	KCNC2	NET1	
	NDUFB8	KDM6B	NFE2L2	
	NDUFB9	KLF2	NME8	
	NDUFC1	KLF4	NOS3	
	NDUFC2	KPNA4	NQO1	
	NDUFS1	LCN2	NR4A3	
	NDUFS2	LDHA	OSER1	
	NDUFS3	LRRK2	PARK7	
	NDUFS4	MAP1LC3A	PAWR	
	NDUFS5	MAP3K5	PAX2	
	NDUFS6	MAPK1	PCGF2	
	NDUFS7	MAPK13	PCNA	
	NDUFS8	MAPK3	PDCD10	
	NDUFV1	MAPK7	PDE8A	
	NDUFV2	MAPK8	PDGFD	
	NDUFV3	MAPK9	PDGFRA	
	PPA1	MAPT	PDK2	
	PPA2	MB	PINK1	
	SDHA	MDM2	PKD2	
	SDHB	MET	PLEKHA1	
	SDHC	MIR103A1	PPARGC1B	
	SDHD	MIR103A2	PPIF	
	TCIRG1	MIR107	PPP5C	
	UQCR10	MIR133A1	PRDX1	
	UQCR11	MIR133A2	PRDX2	
	UQCRB	MIR17	PRDX3	
	UQCRC1	MIR21	PRDX5	
	UQCRC2	MIR34A	PRKAA1	
	UQCRFS1	MIR92A1	PRKCD	
	UQCRH	MIR92A2	PSAP	

	UQCRHL	MIRLET7B	PTPRK	
	UQCRQ	MMP2	PXN	
		MMP3	PYCR1	
		MMP9	RACK1	
		MPO	RELA	
		MPV17	RGN	
		MT-ND5	RHOB	
		MT-ND6	RIPK1	
		MT3	RIPK3	
		MTR	RNF112	
		MYB	ROMO1	
		NCF1	RPS3	
		NET1	SETX	
		NFE2L2	SIGMAR1	
		NME8	SIRPA	
		NOS3	SIRT1	
		NQO1	SMPD3	
		NR4A3	SOD1	
		NUDT15	SOD2	
		OSER1	SOD3	
		PARK7	SRC	
		PAWR	STAT6	
		PAX2	STK25	
		PCGF2	STK26	
		PCNA	SZT2	
		PDCD10	TNF	
		PDE8A	TNFAIP3	
		PDGFD	TP53	
		PDGFRA	TPM1	
		PDGFRB	TRAF2	
		PDK2	TRAP1	
		PINK1	TREX1	
		PKD2	TRPC6	
		PLEKHA1	TRPM2	
		PLK3	TXN	
		PPARGC1A	UCP1	
		PPARGC1B	ZNF277	
		PPIF	ZNF580	
		PPP1R15B		
		PPP2CB		
		PPP5C		
		PRDX1		
		PRDX2		
		PRDX3		
		PRDX5		
		PRKAA1		

		PRKCD		
		PSAP		
		PTK2B		
		PTPRK		
		PTPRN		
		PXN		
		PYCR1		
		RACK1		
		RELA		
		RGN		
		RHOB		
		RIPK1		
		RIPK3		
		RNF112		
		ROMO1		
		RPS3		
		S100A7		
		SCGB1A1		
		SDC1		
		SESN1		
		SESN2		
		SESN3		
		SETX		
		SIGMAR1		
		SIRPA		
		SIRT1		
		SLC8A1		
		SMPD3		
		SOD1		
		SOD2		
		SOD3		
		SRC		
		STAR		
		STAT1		
		STAT6		
		STK24		
		STK25		
		STK26		
		SZT2		
		TNF		
		TNFAIP3		
		TP53		
		TPM1		
		TRAF2		
		TRAP1		
		TREX1		

		TRPA1		
		TRPC6		
		TRPM2		
		TXN		
		TXNIP		
		TXNRD2		
		UBE3A		
		UCP1		
		UCP3		
		ZNF277		
		ZNF580		

[a]KEGG_GLYCOLYSIS_GLUCONEOGENESIS
[b]KEGG_OXIDATIVE_PHOSPHORYLATION
[c]GO_RESPONSE_TO_REACTIVE_OXYGEN_SPECIES
[d]GO_CELLULAR_RESPONSE_TO_REACTIVE_OXYGEN_SPECIES
[e]HALLMARK_REACTIVE_OXYGEN_SPECIES_PATHWAY
All gene sets were obtained from Molecular Signatures Database (MSigDB) v7.1 (14)

Table S3. List of genes in angiogenesis and VEGF signaling pathway signatures.

HALLMARK ANGIOGENESIS	GO ANGIOGENESIS	KEGG VEGF SIGNALING PATHWAY	BIOCARTA VEGF PATHWAY
APOH	AAMP	AKT1	ARNT
APP	ACVR1	AKT2	EIF1
CCND2	ACVRL1	AKT3	EIF1AX
COL3A1	ADAM15	BAD	EIF2B1
COL5A2	ADAM8	CASP9	EIF2B2
CXCL6	ADIPOR2	CDC42	EIF2B3
FGFR1	ADM2	CHP	EIF2B4
FSTL1	AGGF1	CHP2	EIF2B5
ITGAV	AIMP1	HRAS	EIF2S1
JAG1	ANG	HSPB1	EIF2S2
JAG2	ANGPT1	JMJD7-PLA2G4B	EIF2S3
KCNJ8	ANGPT2	KDR	ELAVL1
LPL	ANGPT4	KRAS	FLT1
LRPAP1	ANGPTL3	MAP2K1	FLT4
LUM	ANGPTL4	MAP2K2	HIF1A
MSX1	ANGPTL6	MAPK1	HRAS
NRP1	ANPEP	MAPK11	KDR
OLR1	ANXA2	MAPK12	NOS3
PDGFA	APOD	MAPK13	PIK3CA
PF4	APOLD1	MAPK14	PIK3CG
PGLYRP1	ARHGAP22	MAPK3	PIK3R1
POSTN	ARHGAP24	MAPKAPK2	PLCG1

PRG2	ATP5B	MAPKAPK3	PRKCA
PTK2	ATPIF1	NFAT5	PRKCB
S100A4	B4GALT1	NFATC1	PTK2
SERPINA5	BAK1	NFATC2	PXN
SLCO2A1	BAX	NFATC3	SHC1
SPP1	BCAS3	NFATC4	VEGFA
STC1	BMP4	NOS3	VHL
THBD	BMPER	NRAS	
TIMP1	C19orf10	PIK3CA	
TNFRSF21	C1GALT1	PIK3CB	
VAV2	CALCRL	PIK3CD	
VCAN	CAV1	PIK3CG	
VEGFA	CCBE1	PIK3R1	
VTN	CCL2	PIK3R2	
	CD34	PIK3R3	
	CDC42	PIK3R5	
	CDH13	PLA2G10	
	CEACAM1	PLA2G12A	
	CIB1	PLA2G12B	
	CLIC4	PLA2G1B	
	COL15A1	PLA2G2A	
	COL18A1	PLA2G2C	
	COL4A1	PLA2G2D	
	COL4A2	PLA2G2E	
	COL8A1	PLA2G2F	
	COL8A2	PLA2G3	
	CSPG4	PLA2G4A	
	CTGF	PLA2G4B	
	CTNNB1	PLA2G4E	
	CX3CL1	PLA2G5	
	CXCL17	PLA2G6	
	CXCR3	PLCG1	
	CXCR7	PLCG2	
	CYP1B1	PPP3CA	
	CYR61	PPP3CB	
	DAB2IP	PPP3CC	
	DLL1	PPP3R1	
	DLL4	PPP3R2	
	E2F7	PRKCA	
	E2F8	PRKCB	
	ECM1	PRKCG	
	ECSCR	PTGS2	
	EDN1	PTK2	

	EDNRA	PXN	
	EFNA1	RAC1	
	EFNB2	RAC2	
	EGF	RAC3	
	EGFL7	RAF1	
	EGR3	SH2D2A	
	EIF2AK3	SHC2	
	ELK3	SPHK1	
	ENG	SPHK2	
	ENPEP	SRC	
	EPAS1	VEGFA	
	EPGN		
	EPHA1		
	EPHA2		
	EPHB1		
	EPHB2		
	EPHB3		
	EPHB4		
	ERAP1		
	EREG		
	ESM1		
	ETS1		
	FAM105B		
	FAP		
	FGF1		
	FGF10		
	FGF18		
	FGF2		
	FGF6		
	FGF8		
	FGF9		
	FGFR1		
	FGFR2		
	FIGF		
	FLT1		
	FLT4		
	FMNL3		
	FN1		
	FOXC2		
	FZD5		
	FZD8		
	GBX2		
	GDF2		

	GJA5		
	GNA13		
	GPI		
	GPLD1		
	GPR124		
	GPR4		
	GPR56		
	GPX1		
	GREM1		
	HAND1		
	HAND2		
	HEY1		
	HIF1A		
	HIF3A		
	HMOX1		
	HOXA3		
	HOXA7		
	HOXB13		
	HOXB3		
	HPSE		
	HRG		
	HS6ST1		
	HSPG2		
	HTATIP2		
	ID1		
	IL18		
	IL8		
	ITGA5		
	ITGAV		
	ITGB1		
	ITGB1BP1		
	ITGB3		
	JAG1		
	JAM3		
	JMJD6		
	JUN		
	KDR		
	KLF5		
	KRIT1		
	LAMA5		
	LEF1		
	LEP		
	LEPR		

	LOXL2		
	LRP5		
	MAPK14		
	MCAM		
	MED1		
	MEIS1		
	MEOX2		
	MFGE8		
	MMP14		
	MMP19		
	MMP2		
	MMRN2		
	MYH9		
	NAA15		
	NCL		
	NDNF		
	NFATC4		
	NOS3		
	NOTCH1		
	NOTCH3		
	NOTCH4		
	NOV		
	NOX1		
	NOX5		
	NR4A1		
	NRARP		
	NRCAM		
	NRP1		
	NRP2		
	NRXN1		
	NRXN3		
	NUS1		
	OVOL2		
	PARVA		
	PDCD10		
	PDCD6		
	PDCL3		
	PDE3B		
	PDGFA		
	PDGFRA		
	PDGFRB		
	PGF		
	PIK3CA		

	PIK3CB		
	PIK3CG		
	PIK3R6		
	PITX2		
	PKNOX1		
	PLAU		
	PLCD1		
	PLCD3		
	PLXDC1		
	PLXND1		
	PNPLA6		
	POFUT1		
	PRCP		
	PRKCA		
	PRKD1		
	PRKD2		
	PRKX		
	PROK1		
	PROK2		
	PTEN		
	PTGS2		
	PTK2		
	PTK2B		
	PTPRB		
	RAMP1		
	RAMP2		
	RAPGEF3		
	RASIP1		
	RBM15		
	RBPJ		
	RHOB		
	RNF213		
	ROBO1		
	ROBO4		
	RORA		
	RSPO3		
	S100A7		
	S1PR1		
	SAT1		
	SCG2		
	SEMA3E		
	SEMA4A		
	SEMA5A		

	SERPINE1		
	SETD2		
	SFRP2		
	SH2D2A		
	SHB		
	SHC1		
	SHH		
	SIRT1		
	SLC12A6		
	SLIT2		
	SOX17		
	SOX18		
	SPI1		
	SRF		
	SRPK2		
	SRPX2		
	STAB2		
	STK4		
	SYK		
	TAL1		
	TBX1		
	TBX20		
	TBX4		
	TCF21		
	TDGF1		
	TEK		
	TGFB2		
	TGFBI		
	TGFBR1		
	TGFBR2		
	THBS1		
	THSD7A		
	THY1		
	TIE1		
	TMEM100		
	TMPRSS6		
	TNFAIP2		
	TNFRSF12A		
	TNFSF12		
	TSPAN12		
	TYMP		
	UBP1		
	UNC5B		

	VASH1		
	VAV2		
	VAV3		
	VEGFA		
	VEGFB		
	VEGFC		
	VEZF1		
	WARS		
	WASF2		
	WNT7A		
	XBP1		
	ZC3H12A		
	ZNF304		

All gene sets were obtained from Molecular Signatures Database (MSigDB) v7.1 (14)

Table S4. Epithelial-to-mesenchymal transition, integrated stress response and STAT3 genes.

EMT (16)	**STAT3 signaling** (17)	**Integrated stress response** (18)
ANKRD22	MCL1	ATF3
ANTXR2	JUNB	CHAC1
AP1M2	BCL6	CHOP
AXL	NFIL3	REDD1
BSPRY	CAPN2	
C1orf116	EGR1	
C1orf172	VEGF	
C3orf21	PTPCAAX1	
CARD6	KLF4	
CDH1	EXT1	
CDH3	NPC1	
CDS1	PAK2	
CLDN4		
CLDN7		
CRB3		
DSP		
ELMO3		
ENPP5		
EPB41L5		
EPHA1		

EPN3		
EPPK1		
ERBB3		
EVPL		
F11R		
FN1		
FXYD3		
GALNT3		
GALNT5		
GPR110		
GPR56		
GRHL1		
GRHL2		
HNMT		
INADL		
ITGB6		
KLC3		
KRT19		
KRTCAP3		
LIX1L		
LRRC54		
MAL2		
MAPK13		
MMP2		
MPP7		
MPZL2		
MTAC2D1		
MUC1		
NRP1		
PPARG		
PRR5		
PRSS22		
PRSS8		
RAB25		
RBM35A		
RBPMS		
S100A14		
SCNN1A		
SERINC2		
SH3YL1		
SHROOM3		
SPINT2		
SSH3		

ST14		
STAP2		
TACSTD1		
TACSTD2		
TGFBI		
TJP3		
TMC4		
TMEM125		
TMEM30B		
TMEM45B		
TNFRSF21		
VIM		
ZEB1		

SUPPLEMENTARY REFERENCES

1. Copay AG, Subach BR, Glassman SD, Polly DW, Schuler TC. Understanding the minimum clinically important difference: a review of concepts and methods. Spine J. 2007;7:541–6.

2. Okamoto S, Shiga T, Yasuda K, Ito YM, Magota K, Kasai K, et al. High Reproducibility of Tumor Hypoxia Evaluated by 18F-Fluoromisonidazole PET for Head and Neck Cancer. J Nucl Med. 2013;54:201–7.

3. McGowan DR, Skwarski M, Bradley KM, Campo L, Fenwick JD, Gleeson FV, et al. Buparlisib with thoracic radiotherapy and its effect on tumour hypoxia: A phase I study in patients with advanced non-small cell lung carcinoma. Eur J Cancer. 2019;113:87–95.

4. McGowan DR, Skwarski M, Papiez BW, Macpherson RE, Gleeson FV, Schnabel JA, et al. Whole tumor kinetics analysis of 18F-fluoromisonidazole dynamic PET scans of non-small cell lung cancer patients, and correlations with perfusion CT blood flow. EJNMMI Research. 2018;8:73.

5. Papież BW, Heinrich MP, Fehrenbach J, Risser L, Schnabel JA. An implicit sliding-motion preserving regularisation via bilateral filtering for deformable image registration. Med Image Anal. 2014;18:1299–311.

6. Sahani DV, Kalva SP, Hamberg LM, Hahn PF, Willett CG, Saini S, et al. Assessing Tumor Perfusion and Treatment Response in Rectal Cancer with Multisection CT: Initial Observations. Radiology. 2005;234:785–92.

7. Heinrich MP, Jenkinson M, Brady M, Schnabel JA. MRF-based deformable registration and ventilation estimation of lung CT. IEEE Trans Med Imaging. 2013;32:1239–48.

8. Tofts PS. Modeling tracer kinetics in dynamic Gd-DTPA MR imaging. J Magn Reson Imaging. 1997;7:91–101.

9. Orton MR, d'Arcy JA, Walker-Samuel S, Hawkes DJ, Atkinson D, Collins DJ, et al. Computationally efficient vascular input function models for quantitative kinetic modelling using DCE-MRI. Phys Med Biol. 2008;53:1225–39.

10. Achanta R, Shaji A, Smith K, Lucchi A, Fua P, Süsstrunk S. SLIC superpixels compared to state-of-the-art superpixel methods. IEEE Trans Pattern Anal Mach Intell. 2012;34:2274–82.

11. Rademakers SE, Lok J, van der Kogel AJ, Bussink J, Kaanders JH. Metabolic markers in relation to hypoxia; staining patterns and colocalization of pimonidazole, HIF-1α, CAIX, LDH-5, GLUT-1, MCT1 and MCT4. BMC Cancer. 2011;11:167.

12. Buffa FM, Harris AL, West CM, Miller CJ. Large meta-analysis of multiple cancers reveals a common, compact and highly prognostic hypoxia metagene. Br J Cancer. 2010;102:428–35.

13. Harris AL. Hypoxia — a key regulatory factor in tumour growth. Nature Reviews Cancer. 2002;2:38–47.

14. Liberzon A, Birger C, Thorvaldsdóttir H, Ghandi M, Mesirov JP, Tamayo P. The Molecular Signatures Database (MSigDB) hallmark gene set collection. Cell Syst. 2015;1:417–25.

15. Winter SC, Buffa FM, Silva P, Miller C, Valentine HR, Turley H, et al. Relation of a Hypoxia Metagene Derived from Head and Neck Cancer to Prognosis of Multiple Cancers. Cancer Res. 2007;67:3441–9.

16. Byers LA, Diao L, Wang J, Saintigny P, Girard L, Peyton M, et al. An Epithelial–Mesenchymal Transition Gene Signature Predicts Resistance to EGFR and PI3K Inhibitors and Identifies Axl as a Therapeutic Target for Overcoming EGFR Inhibitor Resistance. Clin Cancer Res. 2013;19:279–90.

17. Alvarez JV, Febbo PG, Ramaswamy S, Loda M, Richardson A, Frank DA. Identification of a genetic signature of activated signal transducer and activator of transcription 3 in human tumors. Cancer Res. 2005;65:5054–62.

18. Stevens AM, Xiang M, Heppler LN, Tošić I, Jiang K, Munoz JO, et al. Atovaquone is active against AML by upregulating the integrated stress pathway and suppressing oxidative phosphorylation. Blood Adv. 2019;3:4215–27.